

Dust environment of an airless object: A phase space study with kinetic models

*Kallio, E., S. Dyadechkin, S. Fatemi, M. Holmström, Y. Futaana,
P. Wurץ, V. A. Fernandes, F. Álvarez, J. Heilimo, R. Jarvinen, W. Schmidt, A.-M. Harri,
S. Barabash, J. Mäkelä, N. Porjo and M. Albo*

Table of Contents

Abstract.....	1
1. Introduction	2
2. Description of the DPEM modelling suite	4
2.1. Hybrid model.....	5
2.2. Electrostatic PIC model	5
2.3. Monte Carlo model	7
2.3.1 Debye layer region	8
2.3.2 3D MC model.....	9
3 Phase space and the role of the Debye layer	12
3.1 Charge and initial velocity of a dust particle	13
4. Discussion.....	14
5. Summary	16
References	16
Figure Captions	20

Abstract

Dust above the lunar surface is important for both science and technology. Dust particles are electrically charged due to impact of the solar radiation and the solar wind plasma and, therefore, they affect the plasma above the lunar surface. Dust is also a health hazard for crewed missions because micron and sub-micron sized dust particles can be toxic and harmful to the human body. Dust also causes malfunctions in mechanical devices and is therefore a risk for spacecraft and instruments on the lunar surface.

Properties of dust particles above the lunar surface are not fully known. However it can be stated that their large surface area due to the irregular shape, the broken chemical bonds on the surface of each dust particle, together with the reduced lunar environment cause the dust particles to be chemically very reactive. One critical unknown factor is the electric field and the electric potential near the lunar surface. We have developed a modelling suite, DPEM (Dusty Plasma Environments: near-surface characterization and Modelling), to study dust environments of the Moon and other airless bodies globally and locally. The DPEM model combines three independent kinetic models: (1) a 3D hybrid

40 model, where ions are modelled as particles and electrons are modelled as a charge neutralizing fluid,
41 (2) a 2D electrostatic Particle-in-Cell (PIC) model where both ions and electrons are treated as particles,
42 and (3) a 3D Monte Carlo (MC) model where dust particles are modelled as test particles. The models
43 are linked to each other unidirectionally: The hybrid model provides upstream plasma parameters to be
44 used as boundary conditions for the PIC model which generates the surface potential for the MC
45 model.

46
47 We have used the DPEM model to study properties of dust particles injected from the surface of airless
48 objects the Moon, the Martian moon Phobos and the asteroid RQ36. We have performed a $(v_0, m/q)$ -
49 phase space study where the property of dust particles at different initial velocity (v_0) and initial mass
50 per charge (m/q) ratio was analysed. Especially, the study identifies regions in the phase space where the
51 electric field within the Debye layer becomes important compared with the gravitational force.
52 Properties of the dust particles in the phase space region where the electric field plays an important role
53 are studied by a 3D Monte Carlo model.

54
55 The current DPEM modelling suite does not include models of how dust particles are initially injected
56 from the surface. Therefore, the presented phase space study cannot give absolute 3D dust density
57 distributions around the analysed airless objects without an additional emission model, which
58 determines how many dust particles are emitted at various places on the analysed $(v_0, m/q)$ -phase space.
59 However, the study identifies phase space regions where the electric field within the Debye layer plays
60 an important role for dust particles. Overall, the shown initial results indicate that when a realistic dust
61 emission model is available, the unified DPEM modelling suite is a powerful tool to study the dust
62 environments of airless bodies such as moons, Mercury, asteroids and non-active comets far from the
63 Sun.

64
65

66 1. Introduction

67
68 The Moon is the best known example of the so-called direct plasma-surface interaction where plasma
69 interacts directly with the surface of the object. This direct interaction takes place at the lunar surface
70 because the Moon has neither an atmosphere nor a global intrinsic magnetic field, which could change
71 the motion of charged particles near the surface. The direct plasma-surface interaction makes the Moon
72 an ideal object to study various physical processes near the surface, which are anticipated to take place
73 on the so called airless bodies, like asteroids, other planetary moons in the Solar System and non-active
74 dusty comets.

75
76 One can anticipate that many physical parameters affect surface processes near the lunar surface (see
77 e.g. Kallio et al., 2012, and discussion therein): First, the density, bulk velocity and temperature of the
78 solar wind protons and electrons; Furthermore, secondary particles (electrons, positively and negatively
79 charged ions) resulting from the impact of the solar wind onto the surface. Third, photoelectrons from
80 the surface in places exposed to the sunlight; Fourth, charged dust particles above the surface, which
81 are also sinks and sources of charged particles like the surface itself; Fifth, the interplanetary magnetic
82 field (IMF), the magnetic field associated with the Earth's magnetosheath or with the magnetosphere.
83 Furthermore, possible local magnetic anomalies affect the properties of plasma, for example, reflection
84 of the solar wind electrons and protons from and above the surface requiring e.g. hybrid modelling
85 beyond the Debye scale; Sixth, the convective electric field associated with the flow of the solar wind,
86 with the electric field in the Earth's magnetosheath or in the magnetosphere (e.g. Kallio and Facskó,
87 2015), in addition to the electric field within the Debye sheath (or the Debye layer) where the plasma is
88 not quasi-neutral. Furthermore, the solar radiation varies due to temporal variations of the Sun. The

89 intensity of the solar radiation at a given point on the lunar surface varies also along the orbit of the
90 Moon around the Earth. Moreover, physical and chemical properties of the locations on the lunar
91 surface from where the charged particles originate vary (e.g., basalt flows or crustal material). Finally,
92 surface processes are affected by topographical variations due to lunar landscapes (e.g. Dyadechkin et
93 al., 2015).

94
95 In addition to the aforementioned physical parameters and processes the lunar near-surface region is
96 highly interesting for basic space plasma physics research. Such research is also needed to improve the
97 understanding of the interaction between the dust particles on the lunar surface and the Debye layer
98 that directly affect the technical and scientific instrumentation deployed on the lunar surface during
99 different missions and pose ultimately a potential hazard to humans (e.g. Linnarsson et al., 2012). In
100 addition, laboratory experiments have shown that dust particles can migrate due to the electric field
101 near the surface [Wang et al., 2010]. Such dust particles may cause malfunctions of moving spacecraft
102 parts or space instruments on the lunar surface. Moreover, dust can contaminate astronomical
103 observations in the infra-red, visible and UV wavelength ranges [Murphy and Vondrak, 1993; Stubbs et
104 al., 2006]. Lunar dust has also been observed far above the surface (see e.g. references in Stubbs et al.,
105 2006) suggesting that dust may have global effects.

106
107 Space weathering caused by micrometeorites, galactic cosmic rays and solar energetic particles erode,
108 and vaporize dust grains and regolith on the lunar surface (see e.g. Jordan et al., 2015). However, the
109 difference between dust on the Earth and on the Moon is that there is no Earth-like erosion of dust
110 particles caused by wind or water on the lunar surface. Therefore, small dust particles can have very
111 sharp edges and reactive broken chemical bonds (e.g. Liu and Taylor, 2011; Liu et al., 2008; Linnarsson
112 et al., 2012). When entered into the lungs of an astronaut, the small sharp dust particles are therefore a
113 potential health hazard. Generally speaking, lunar dust is more chemically reactive, has large surface
114 areas, and is composed of sharper jagged edges than Earth's dust [Cain, 2010]. Properties of dust are
115 therefore a critical issue that has to be taken into account when a crewed lunar mission is planned.

116
117 A comprehensive lunar dust model should consider three different space regimes. It should include (1)
118 a global model that gives properties of the solar wind plasma impacting on the surface, (2) a local
119 model of the electric field above the lunar surface which accelerates dust particles, and (3) a global
120 model which gives the density of dust around the Moon. Toward this goal, three different connected
121 models are developed in this work. A global hybrid model gives the properties of protons above the
122 surface. A local 2D full kinetic model is then used to derive the surface potential at different Solar
123 Zenith Angles (SZA) near the surface. Finally, a global Monte Carlo model is used to derive three
124 dimensional densities of the dust particles escaping from the surface. The developed modelling suite is
125 used to study the 3D dust density profiles at the Moon, the Martian moon Phobos and the asteroid
126 RQ36 to cover a large size range of planetary objects.

127
128 The paper is organized as follows. First the three developed models are described. The capacity of the
129 models are demonstrated with a parameter study where the models are used to derive 3D dust densities
130 for the Moon, Phobos and the asteroid RQ36 for manually given input parameters and two different
131 dust emission models: A homogeneous dust emission for the surface and a point source at the subsolar
132 point. In the presented parameter study initial parameters for the dust particles were chosen in a range
133 which makes it possible to analyse effects of the surface potential and, consequently, the capacity of the
134 developed modelling suite to study various airless bodies. Finally, lessons of the analysed cases and a
135 roadmap for future more sophisticated dust models are discussed.

136
137

138 2. Description of the DPEM modelling suite

139

140 The DPEM model contains three kinetic models: (1) a 3D Hybrid model where ions are particles and
141 electrons form a fluid, (2) a 2D electrostatic full kinetic Particle-in-Cell (PIC) model where both ions
142 and electrons are particles, and (3) a 3D Monte Carlo (MC) model.

143

144 Figure 1 shows an illustration of the models and depicts how they are connected to each other by
145 unidirectional connections where the hybrid model provides the plasma parameter boundary conditions
146 for the PIC model, which in turn gives inputs to the MC model. More precisely, the hybrid model
147 provided the positions and velocities of the solar wind protons which hit the surface of the planetary
148 object. The PIC model uses these particles and derives the macroscopic plasma parameters associated
149 with the precipitating protons: the density of protons, $n(\text{H}^+)$, three bulk velocity components for
150 protons ($U_x(\text{H}^+)$, $U_y(\text{H}^+)$, $U_z(\text{H}^+)$) and the temperatures of protons in three directions ($T_x(\text{H}^+)$, $T_y(\text{H}^+)$,
151 $T_z(\text{H}^+)$). Here the indices refer to the Object-centred Solar wind Orbital (OSO) coordinates where the
152 x -axis points from the centre of the (spherical) object against the flow of the solar wind, the y -axis
153 shows the direction of the velocity vector of the object perpendicular the x -axis, and the z -axis
154 completes the right handed coordinate system. All three models include their own 3D Maxwellian
155 Particle Generator, MPG, which are used to inject particles into models. If the macroscopic parameters
156 associated with the precipitating protons are close to the values of the undisturbed solar wind
157 parameters, as in the cases analysed in this paper as discussed later in Section 2.1, the PIC model
158 generates particles by using its own MPG which uses undisturbed plasma parameters. Finally, the PIC
159 model gives the surface potential values to the MC model which uses the potential values in its MPG as
160 will be discussed later in detail in Section 2.3.2.

161

162 All three models in the DPEM suite are kinetic simulations where some, or all, of the particle species
163 are modelled as particles. The particles are propagated by using Newton's second law:

164

$$165 \quad m \frac{d\mathbf{v}(\mathbf{r},t)}{dt} = m\mathbf{g}(\mathbf{r}) + q\mathbf{E}(\mathbf{r},t) + q\mathbf{v} \times \mathbf{B}(\mathbf{r},t) + \mathbf{F} \quad [1a]$$

$$166 \quad \frac{d\mathbf{r}(\mathbf{r},t)}{dt} = \mathbf{v}(\mathbf{r},t) \quad [1b]$$

167

168 Here, q , m and \mathbf{v} are the charge, mass and velocity of a particle, \mathbf{g} is the gravitation acceleration at the
169 point where the particle is, \mathbf{E} is the electric field, \mathbf{B} the magnetic field and \mathbf{F} is the contribution of all
170 other forces, such as caused by the radiation pressure or collisions. The three models differ from each
171 other in the way particles are modelled, how the electric field is derived and how the magnetic field is
172 treated.

173

174 The objects were assumed to be spherical balls with a homogeneous mass density. The DPEM model
175 was used to study three different objects of different sizes, masses and escape velocities:

176

177 1. *Object No1: Near Earth asteroid RQ36*

178

179 The RQ36, or 101955 Benu, is an Apollo near Earth asteroid discovered in 1999. In the
180 simulations RQ36 was assumed to have a radius of 252 m and a mass of 1.4×10^{11} kg. The
181 escape velocity from RQ36 is about 0.2 m/s.

182

183 2. *Object No2: Martian moon Phobos*

184

185 Phobos was assumed to have radius of 12 km and the mass of 1.066×10^{16} kg. Escape velocity
186 from Phobos is about 11 m/s and the surface gravity is 0.0057 m/s^2 . In the simulations Phobos
187 was assumed to be in the solar wind.

186

187 3. *Object No3: The Moon.*

188 In the global simulations the Moon was assumed to be in the solar wind and have a radius of
 189 1730 km and a mass of 7.35×10^{22} kg. The escape velocity from the Moon is about 2.5 km/s and
 190 the surface gravity is 1.622 m/s^2 .

191
 192 Moreover, in the PIC model the EUV light is directed along the x -axis, which results in photoelectron
 193 emission from the surface. Photoelectrons were modelled by a 3D Maxwellian velocity distribution
 194 function with the thermal velocity of 621 km/s, which corresponds to a temperature of about 2.2 eV.
 195 The photoelectron emission current density was assumed to be $4.5 \mu\text{Am}^{-2}$ based on measurements
 196 [Willis et al., 1973] and which has been used in previous 1D PIC simulations (see, e.g., Poppe and
 197 Horányi, 2010). Moreover, the high energy tail of the Maxwellian velocity distribution function was cut
 198 away by removing electrons above 6 eV.
 199

200 2.1. Hybrid model

201
 202 In the hybrid model, ions are modelled as particles according to Eqs. 1-2. Electrons are modelled as a
 203 massless fluid. The charge density of electrons, n_e , is assumed to be equal to the total charge density of
 204 positively charged ions, that is, the plasma is assumed to be quasi-neutral. In the DPEM hybrid model
 205 the only positively charged ions were the solar wind protons. The electric field is derived from the
 206 electron momentum equation and the definition of the electric current:

$$207 \quad \mathbf{E}(\mathbf{r}, t) = -\mathbf{U}_e(\mathbf{r}, t) \times \mathbf{B}(\mathbf{r}, t) \quad [2a]$$

$$208 \quad \mathbf{U}_e(\mathbf{r}, t) = \mathbf{U}_{H^+}(\mathbf{r}, t) - \mathbf{j}(\mathbf{r}, t) / en_e(\mathbf{r}, t) \quad [2b]$$

209 Here \mathbf{U}_e , \mathbf{U}_{H^+} , \mathbf{j} and e are the electron bulk velocity, bulk velocity of protons, the electric current, and
 210 the positive unit charge, respectively (see e.g. Kallio, 2005, for the details of a 3D hybrid model
 211 simulations for a Moon-type of airless objects without an intrinsic magnetic field). The object is
 212 assumed to be an insulator (resistivity 1×10^7 ohm/m) into which the IMF can diffuse (see Holmström
 213 et al., 2012, for the details of the model). The upstream parameters were $n(H^+) = 7.1 \text{ cm}^{-3}$, $\mathbf{U}(H^+) =$
 214 $[-450, 0, 0] \text{ km/s}$, $T(H^+) = 1.2 \times 10^5 \text{ K}$ and the IMF was $\mathbf{B} = [7/\sqrt{2}, 7/\sqrt{2}, 0] \text{ nT}$.

215
 216 Figure 2 shows a snapshot of the magnetic field magnitude obtained from the hybrid model run for the
 217 Moon. In the run the grid cell size was $200 \times 200 \times 200 \text{ km}^3$. The simulation domain size is 12000 km
 218 along the x -axis, and 8000 km along the y - and z -axis. An important feature in the Moon case is that the
 219 IMF diffuses into the body and no bow shock is formed upstream of the object. Therefore, the solar
 220 wind is practically undisturbed on the dayside ($\text{SZA} < 90^\circ$). On the nightside a long magnetic wake is
 221 formed, as seen in Fig. 2, and the nightside region ($\text{SZA} > 90^\circ$) is highly distorted.
 222
 223

224 2.2. Electrostatic PIC model

225
 226 In the electrostatic PIC simulation both ions and electrons are modelled as particles. In contrast to the
 227 hybrid model the plasma is not assumed to be quasi-neutral and, consequently, charge separation can
 228 exist. In the PIC model the external force \mathbf{F} in Eq. 1a includes only the gravitational force. The electric
 229 field is derived from the electric potential (Eq. 3), ϕ , which in turn is obtained from the total electric
 230 charge density, ρ_q , from the Poisson's equation (Eq. 4):

$$231 \quad \mathbf{E}(\mathbf{r}, t) = -\nabla\phi(\mathbf{r}, t) \quad [3]$$

232
$$\nabla^2 \varphi(\mathbf{r}, t) = -\rho_q(\mathbf{r}, t)/\epsilon_0 \quad [4]$$

233 Here ϵ_0 is the electric permittivity of free space. As already mentioned, in the runs presented in this
 234 paper the PIC model was electrostatic, that is, the magnetic field was not assumed to have a time
 235 dependency. Moreover, in the analysed PIC simulations the magnetic field was assumed to be zero. The
 236 boundary condition on the solar wind wall at $x = 100$ m is that the electric field is zero, therefore, the
 237 electric potential is a constant. The length of the cell was 0.25 m.

238 The architecture of the DPEM model enables injection of the protons into the PIC model which have
 239 impacted the surface in the hybrid model. The properties of precipitating protons were tested by
 240 studying in a hybrid model a situation where density, bulk velocity and the thermal velocity of the solar
 241 wind was 7.1 cm^{-3} , $[-450, 0, 0] \text{ km/s}$ and $1.2 \times 10^5 \text{ K}$, respectively. The IMF was assumed to be $[-4.95,$
 242 $+4.95, 0] \text{ nT}$. The plasma density, n , three bulk velocity components, (U_x, U_y, U_z) , and three
 243 temperature components, (T_x, T_y, T_z) , were derived at the three objects by using the algorithms (see. e.g.
 244 analysis in Kallio et al., 1997)

$$n = \frac{R}{dTdA} \sum_i \frac{w_i}{|\mathbf{v}_i \cdot \mathbf{r}_i|} \quad [5a]$$

$$\mathbf{U} = \sum_i \mathbf{v}_i \frac{w_i}{|\mathbf{v}_i \cdot \mathbf{r}_i|} / \sum_i \frac{w_i}{|\mathbf{v}_i \cdot \mathbf{r}_i|} \quad [5b]$$

$$T_k = \frac{m_p}{k_B} \sum_i (\mathbf{v}_{ki} - \mathbf{U}_k)^2 \frac{w_i}{|\mathbf{v}_i \cdot \mathbf{r}_i|} / \sum_i \frac{w_i}{|\mathbf{v}_i \cdot \mathbf{r}_i|} \quad [5c]$$

245 Here R is the radius of the object, $\mathbf{r}_i = (x_i, y_i, z_i)$ is the position vector where the ion i hits the surface, \mathbf{v}_i
 246 $= (v_{xi}, v_{yi}, v_{zi})$: the velocity vector of an ion i which hits the sphere, $dA_{\text{collected}}$ is the area on the sphere from
 247 where the particles were collected on the surface, $dT_{\text{collected}}$ is the particle accumulation time, m_p is the
 248 mass of a protons and k_B is the Boltzmann's constant. The sum is over all particles that hit the surface
 249 $dA_{\text{collected}}$ during a time interval $dT_{\text{collected}}$. The subscript k in Eq. 5c shows the component of the velocity,
 250 i.e. x, y or z . The particles were collected in 10° SZA angle bins from SZA = 0° up to the SZA where
 251 the last hit on the surface was recorded. For the Moon, Phobos and asteroid RQ36 $dT_{\text{collected}}$ was 50s, 10s
 252 and 0.3226s, respectively.

253 An important feature of the derived parameters was that the plasma parameters on the dayside were
 254 much like in the undisturbed solar wind. Another important feature is that there were no hits of H^+
 255 ions on the surface of the Moon, Phobos and RQ36 at SZA values larger than $\sim 107^\circ$, $\sim 105^\circ$ and
 256 $\sim 105^\circ$, respectively (c.f. Fig. 3d). This limitation is related to the fact that the hybrid model assumes
 257 quasi-neutrality while in reality a charge separation takes place on the nightside, which results in an
 258 ambipolar electric field accelerating protons deep into the tail (see e.g. Kallio et al., 2005, and ref.
 259 therein). Moreover, the number of precipitating particles decrease rapidly at SZA $> 90^\circ$ which causes
 260 statistical fluctuations to the estimation of the particle density (Fig. 3a) and particle temperature (Fig.
 261 3c). This result indicates that the hybrid model cannot give accurate plasma parameters on the nightside
 262 near the surface for the PIC simulation. Therefore, only the dayside region is analysed in this paper
 263 with the PIC model and the plasma was assumed to be undisturbed. Note that non-disturbed plasma
 264 parameters on the surface are, indeed, expected to exist because objects in the hybrid model absorb
 265 particles and let the IMF diffuse inside them without the formation of an obstacle or a bow shock
 266 above the surface (c.f. Fig. 2).

267 Localised 2D PIC simulations were made for six different SZA values (0° , 15° , 30° , 45° , 60° and 75°)
268 assuming that the surface is a plane. The Moon is assumed to be in the nominal solar wind where the
269 density, the bulk velocity, and the kinetic temperature of the undisturbed solar wind protons were 10
270 cm^{-3} , 400 km/s and 10 eV , respectively. The bulk velocity of electrons was also 400 km/s . The thermal
271 velocity of electrons was $1.36 \times 10^3 \text{ km/s}$, which corresponds to temperatures of about 10.5 eV . The
272 density of the solar wind electrons was adjusted in to have quasi-neutrality on the solar wind wall. The
273 SZA effect was taken into account by multiplying the solar wind velocity and the flux of the
274 photoelectrons by $\cos(SZA)$, i.e., taking into account the velocity component normal to the surface.

275 Fig. 4 shows the electric potential in the analysed cases. All potentials are non-monotonic and have
276 local minimum values where the electric field changes its direction. The electric field points
277 upward/downward below/above the local minimum. This means that positively charged particles are
278 accelerated upward just above the surface and downward near the solar wind wall in the simulation.
279 The most important parameter from the MC modelling point of view is the surface potential. As seen
280 in the Fig. 4, the surface potential decreases with increasing SZA. Moreover, in the analysed cases the
281 surface potential is positive at least up to $SZA = 60^\circ$ and becomes negative between $SZA = 60^\circ$ – 75° .
282 The density of photoelectrons, solar wind electrons, and protons as well as technical details about the
283 developed PIC code can be found in the companion paper [Dyadechkin et al., 2015].
284

285 It is important also to note that in this paper dust particles were assumed to be positively charged. As
286 can be seen in Fig. 4, in the PIC model the electric field points upward at the surface in all analysed
287 SZA values. Moreover, taking into account (1) the boundary condition $\mathbf{E} = 0$ at the solar wind wall (x
288 $= 100 \text{ m}$) and (2) the assumption that there is no electric charge outside of the simulation box, Gauss'
289 law states, that the total electric charge within the PIC simulation box has to be zero. In this situation
290 an upward pointing electric field on the surface indicates that the surface is positively charged. The dust
291 particles in the MC simulation are originating from the surface. Due to EUV light the dust particle
292 surfaces emit photoelectrons like other surface regions and in this paper the dust particles were
293 assumed to be positively charged in the MC model.
294

295 2.3. Monte Carlo model

296
297 In the Monte Carlo model the motion of a dust particle of a mass m_{dust} , an electric charge of q_{dust} , and an
298 initial velocity is influenced by a prescribed force field. In the cases analysed in this paper the forces
299 were the Lorentz force and the gravitational force. In the Moon and asteroid RQ36 simulations the
300 IMF was assumed to be $[-4.95, +4.95, 0.0] \text{ nT}$ and in the Phobos simulations $[-1.63, +2.52, 0.0] \text{ nT}$.
301 The convection electric field was set to zero to investigate change of the energy of the dust particles
302 caused by the surface charging and gravitation.
303

304 The density of the dust was derived from two Monte Carlo models: (1) Dust within and near the Debye
305 layer is studied by a local 2D MC model and the (2) global dust distribution around an object by a 3D
306 MC model. Two different models were used to obtain a good spatial resolution near the surface, where
307 the length scale of the electric potential is the Debye length, and around the object, where the length
308 scale is large, on the order of the radius of an object.
309

310 As will be discussed in detail later in Section 2.3.5., it is not known how large the amount of detached
311 dust particles from the surface can become and what might be their masses, electric charges and the
312 velocity distribution functions. Dust particles can be envisioned to be lifted from the surface by
313 micrometeoroid impacts or by a human activity such as a moving lunar rover or landing of a spacecraft.
314 Dust lifting by electrostatic forces has also been a topic of numerous studies (see e.g. Farrell et al.,
315 2007). The particle flux of dust from the surface is also an unknown parameter.

316
317
318
319
320
321
322
323
324
325
326

Because of the aforementioned uncertainties several choices have been made in the MC simulations to study the sensitivity of the results to the input parameters. First, simulations were made for different masses, charges and velocities of dust particles. Second, the role of the surface charge, which affects the acceleration of charged dust particles, was studied by making runs with and without surface charging. Third, two different dust source models were analysed: A full surface dust emission case and a point source dust emission case. Fourth, the density of the dust is given in normalized values because the particle flux of dust is not known. Fifth, the initial velocity distribution function of dust particles emitted from the surface was assumed to be Maxwellian.

327 2.3.1 Debye layer region

328
329
330
331
332
333
334
335
336

Fig. 5 shows 1D density profiles of dust particles within the Debye layer in at the analysed “cold” case and the “hot” case. In the 2D MC runs the dust particles had the mass of 6.2832×10^{-18} kg ($\sim 3.76 \times 10^9$ amu, where amu is the atomic mass unit \sim the mass of a proton of 1.67×10^{-27} kg), and the electric charge of $+3.5322 \times 10^{-17}$ C (~ 221 e, where e is the positive unit charge of 1.602×10^{-19} C). The adopted dust mass and electric charge has the same order of magnitude as the dust ($\sim 5.3 \times 10^8$ amu, ~ 105 e) which has recently been used to study density of dust above lunar 2D surfaces. They correspond to a dust particle with a radius of ~ 0.05 μm and a potential of ~ 3 V [Dyadechkin et al., 2015].

337
338
339
340
341
342
343

Densities were derived for the six electric potential cases shown earlier in Fig. 4. The densities from the 2D MC model given in Fig. 5 are derived along the x -axis at $y = 0$ m. In the 2D PIC model the x -axis is the vertical axis pointing away from the surface and the y -axis is the horizontal axis. Initial parameters for the dust were chosen to give an example of the situation where the role of the electric potential can be identified in dust densities. The simulated region was $x = [0, 100]$ m, the grid size was 0.25 m, the time step was 0.01 s and the duration of the simulation was 50 s.

344
345
346
347
348
349

The cold dust run is shown in Fig. 5a (*the Run PIC-1*). In this run dust was launched from the surface with a 3D Maxwellian velocity distribution function with a bulk velocity of 10 m/s and thermal velocity of 1 mm/s. In this cold dust case or a “beam” dust case the adopted thermal velocity was therefore much smaller than the bulk velocity and the maximum density value can be found at the altitude where the upward moving velocity changes its direction to downward velocity.

350
351
352
353
354
355

Fig. 5b represents the hot dust case (*the Run PIC-2*) where the thermal velocity of 2 m/s is comparable with the bulk velocity of 10 m/s. Thermal spread results in the situation where dust particles turn back to surface at different altitudes resulting in a spreading of the density around the maximum density. In the hot dust case, as in the cold dust case, the altitude of the maximum dust density decreases with increasing SZA because the surface charging decreases with the increasing SZA.

356
357
358
359
360
361
362
363
364
365

Note that the density differences in Fig. 5a and 5b are caused purely by the Debye layer. In the cold dust case the maximum density forms a sharp peak because all emitted dust particles had quite similar initial velocities. The maximum altitude is highest at small SZA values because the positive surface potential is largest there and, consequently, it gives the maximum upward pointing acceleration for a positively charged dust particle. The SZA = 60° case resembles most the case without the Debye layer because in this SZA situation the surface potential is near zero (c.f. Fig. 4) and, therefore, it has only slightly increased the maximum altitude from about 31 m ($= 0.5 \times (10 \text{ m/s})^2 / 1.622 \text{ m/s}^2$), which they would have had due to the lunar gravitational field alone. The 60° case also divides the density curves into two regions with respect to the SZAs: The SZA case where the (positive) Debye layer increases the maximum altitude and the high SZA case where the maximum altitude is decreased by the Debye layer.

366
367

368 2.3.2 3D MC model

369

370 The 3D dust density distribution function cannot be derived with the similar small grid size as shown in
371 Fig. 5 because of the high computational cost. Therefore, the role of the surface charge was taken into
372 account in the following way. First, the Debye layer region was removed from the 3D MC simulation
373 region. Second, the effect of the removed Debye layer was taken into account by modifying the radial
374 (upward) velocity of a dust particle, which is launched in the MC model at SZA, $v_r^{MC}(SZA)$, by using
375 the surface potential at the launch point, $\varphi_{surf}^{PIC}(SZA)$, which is derived from the PIC model:
376

$$377 \frac{1}{2}m_{dust}v_r^{MC}(SZA)^2 + m_{dust}U(h)_g = \frac{1}{2}m_{dust}v_r^{Maxwell^2} + m_{dust}U(0)_g + q_{dust}\varphi_{surf}^{PIC}(SZA) [6]$$

$$378 \Rightarrow v_r^{MC}(SZA) = v_r^{Maxwell} \sqrt{1 + \frac{2\left(\frac{q_{dust}}{m_{dust}}\right)\varphi_{surf}^{PIC}(SZA) - 2[U(h)_g - U(0)_g]}{v_r^{Maxwell^2}}} [7]$$

379

380 Here $v_r^{Maxwell}$, $U(h)_g$, $U(0)_g$ are the radial velocity component derived from the 3D Maxwellian
381 velocity distribution generator of the MC model, the gravitation potential at the height h from the
382 surface and the gravitational potential on the surface, respectively. The two velocity components along
383 the surface were unchanged by the electric potential. As pointed out before, the properties of
384 precipitating protons at the dayside in all three analysed objects were much like the undisturbed solar
385 wind protons on the dayside. Therefore, similar SZA dependent surface potentials were used for all
386 objects at $SZA < 90^\circ$ as shown in Fig. 4. At higher SZA values the surface potential was assumed to be
387 zero because the hybrid model does not give accurate plasma parameters near the surface, as also noted
388 before.

389

390 It is worth recalling how the surface potential affects the radial velocity in Eq. (7). As discussed in
391 Section 2.2, the surface as well as the dust particles can be regarded as positively charged at $SZA < 60^\circ$.
392 However, a dust particle can also be non-charged because of the low surface charging, as will be
393 discussed in detail later in Section 2.3.5. A situation where a dust particle is positively charged means
394 that the term $q_{dust}\varphi_{surf}^{PIC}(SZA)$ in Eq. (7) is positive at $SZA < 60^\circ$ and, consequently, that a dust
395 particle which has passed through the Debye layer has increased its radial velocity. This also means that
396 the surface potential increases the number of dust particles, which can escape from the Debye layer
397 because low velocity dust particles can get enough energy to move to high altitudes in the gravitational
398 field. At $SZA = 75^\circ$, instead, the surface potential is negative and a positively charged dust particle
399 which has passed through the Debye layer has decreased its radial velocity. Therefore the surface
400 potential decreases the number of small velocity dust particles which can escape from the Debye layer
401 at high SZA values.

402

403 In all 3D MC runs identical upstream parameters were used to see the effect of the size of the object.
404 The 3D MC model used periodic boundary conditions and the grid size was 0.125 times the radius of
405 the object. The time steps in the 3D MC Moon, Phobos and RQ36 runs were 20s, 20s and 1s,
406 respectively.

407

408 2.3.2.1 Asteroid RQ36

409 The first analysed object is the asteroid RQ36. Figure 6 shows the simulated normalized 3D dust
410 densities when the roles of the initial velocity and the mass of a dust particle as well as the dust
411 emission site were studied. In all cases in Fig. 6 the surface potential was assumed to be zero, to study

412 later its role. The charge of the dust particle was +350 e. The four runs, their basic input parameters
413 and the main characteristic features of the solution are the following:

414
415 **1. Run RQ36-1** (Fig. 6a)

416 No surface charging. Dust particles are emitted homogeneously through the entire surface of an
417 object mimicking the situation when the asteroid is within large homogeneous and isotropic
418 micrometeoroid cloud. The mass and the charge of a dust particle were 3.7×10^9 amu and +350
419 e, respectively. The initial bulk velocity in the Maxwellian velocity distribution function of the
420 dust particles was zero but they had a non-zero temperature of 300 K, which corresponds to
421 the thermal speed of about 0.03 m/s ($= \sqrt{k_B T / m_{dust}}$, where k_B is Boltzmann's constant).
422 Dust particles are bound to the surface and do not escape from the asteroid where the escape
423 velocity is 0.2 m/s.

424
425 **2. Run RQ36-2** (Fig. 6b)

426 In this case dust particles are injected from a single source point on the surface, mimicking the
427 localised micrometeorite impact or emission caused by a human/robotic activity on the surface.
428 The particles are injected from the source point that located at $(x, y, z) = (R, R, R)/\sqrt{3}$, where R
429 is the radius of the object, with initial velocity of 0.2 m/s, i.e. equal to the escape velocity. Dust
430 particles can at this high velocity leave the object, while in the *Run RQ36-1* they were all
431 gravitationally bound to the asteroid.

432
433 **3. Run RQ36-3** (Fig. 6c)

434 Simulation parameters for this run are identical to those in the *Run RQ36-2*, except that the
435 mass of the dust particle was 3.7×10^8 amu, i.e., 10 times smaller than in the runs *RQ36-1* and
436 *RQ36-2*. The smaller mass results in a more extended dust cloud around the asteroid.

437
438 **4. Run RQ36-4** (Fig. 6d)

439 In this run dust particles are released from a single point that is located in the x - y -plane at
440 $SZA = 45^\circ$ i.e. at $(x, y, z) = (R, R, 0)/\sqrt{2}$. The initial velocity for the dust particles in this
441 simulation was increased to 0.4 m/s, i.e., to larger values than the escape velocity.

442
443
444 The effects of the surface charge in asteroid RQ36 was studied in Fig. 7. Here the inputs are similar as
445 in the two previous examples but now the surface charge from the PIC model is included. The two new
446 runs are the following.

447
448 **5. Run RQ36-5** (Fig. 7a)

449 Simulation parameters for this run are similar to the *Run RQ36-1* except that the surface
450 potential is now non-zero on the dayside. It can be seen that the surface potential charging has
451 a considerable effect on dust motion near the asteroid, allowing dust particles to escape from
452 the dayside in the analysed initial parameter case. Note that dust particles cannot escape from
453 the nightside because the surface potential in the model was zero there.

454
455 **6. Run RQ36-6** (Fig. 7b)

456 In this example dust particles are released from a single source point on the surface which is on
457 the x - y -plane at $SZA = 45^\circ$. Simulation parameters are similar to the *Run RQ36-4*, except that
458 now the surface charging is included. Similarly as in the *Run RQ36-4*, dust particles have an
459 initial velocity prior to the surface charging. Therefore, the initial velocity of the particles is
460 nearly 10 times larger than the escape velocity from the asteroid. In this case a jet-like stream of
461 escaping dust particles is formed, as seen in Figure 7b.

462

463
464
465
466
467
468
469
470

Overall, comparison of Figs. 6 and 7 illustrates how the surface charging can affect the density distribution of the analysed dust particles. The detailed 3D density distribution depends, however, on the initial properties of the dust particles. Therefore, dust particles with different masses, charges and initial velocities can have very different 3D density profiles. The role of the initial parameters will be discussed later in detail in Section 2.3.4.

471 **2.3.2.2 Phobos moon**

472
473
474
475
476

The Martian moon Phobos is an example of an object with the size between the small asteroid RQ36 and the Moon. Figure 8 shows an example of simulation runs which are similar to those done for the asteroid RQ36.

477 **7. Run Phobos-1 (Fig. 8a)**

478
479
480
481
482
483

This run has similar inputs as the *Run RQ36-1*: Initial velocity, temperature, mass and the charge of dust particles are 0 m/s, 300 K, 3.7×10^9 amu and +350 e, respectively. There is no surface charging and dust was emitted from the entire surface of Phobos. As in the asteroid *Run RQ36-1* case dust particles do not have enough velocity to form an extended dust cloud far above the object.

484 **8. Run Phobos-2 (Fig. 8b)**

485
486
487
488
489

In this run, all the simulation parameters are similar to *Run Phobos-1*, but now the dust emission is from a single point source which is on the x - y -plane at $\text{SZA} = 45^\circ$. Note that the initial velocity of a dust particle ($U = 12.1$ m/s, $T = 5 \times 10^7$ K) is larger than the escape velocity from Phobos (~ 11 m/s). Note also the formation of a dust plume around Phobos.

490 **9. Run Phobos-3 (Fig. 8c)**

491
492
493
494
495

Simulation parameters for this run are similar to the *Run Phobos-1* except that now the non-zero surface charging is included on the dayside. The surface potential is similar to the surface potential applied in *the Run RQ36*. Note how the surface potential accelerates dust particles upward, and a clear 3D dust cloud is formed around Phobos on the dayside.

496 **10. Run Phobos-4 (Fig. 8d)**

497
498
499
500
501
502

Same inputs as in the *Run Phobos-3* but now the mass of a dust grain was reduced from 3.7×10^9 amu to 3.7×10^8 amu. As can be seen in Fig. 8d, the surface potential has resulted in an even more extended 3D dust cloud for these light dust particles.

503 **2.3.2.3 The Moon**

504
505
506
507
508
509
510
511
512

The Moon is larger and much heavier than Phobos and RQ36, thus the surface charging does not provide enough energy for the released dust particles to escape from the lunar gravitational field. Therefore, to see dust far above the surface, dust particles have been assumed to have an initial velocity of 3 km/s, i.e., larger than the escape velocity from the Moon (~ 2.5 km/s). The mass and the charge of dust particles were as in the *Run RQ36-1* (3.7×10^9 amu, +350 e). Figure 9 shows a run where dust particles were emitted at a single point at $\text{SZA} = 0^\circ$. Such emission results in density enhancement on the dayside around the Moon-Sun line.

513 3. Phase space and the role of the Debye layer

514

515 The PIC model has a special role in the DPEM modelling suite because it transfers information from
 516 the hybrid model to the MC model by linking the properties of the 3D plasma environment and the 3D
 517 dust environments. Linking of the hybrid model and the MC model was realized via the surface
 518 potential. The effect of the surface potential on the dust densities has been discussed briefly already in
 519 Section 2.3.2, but it is useful to study it more quantitatively. This can be done by analysing Eq. (7) and
 520 writing it in the form

521

$$522 \quad v_r^{MC}(SZA) = v_r^{Maxwell} \sqrt{1 + c_\phi - c_g} \quad [8a]$$

523

$$523 \quad c_\phi \equiv \frac{E_\phi^{pot}}{E_r^{kin}} = 2 \frac{q_{dust} \phi_{surf}^{PIC}(SZA)}{m_{dust} v_r^{Maxwell}{}^2} \quad [8b]$$

524

$$524 \quad c_g \equiv \frac{E_g^{pot}}{E_r^{kin}} = 2 \frac{m_{dust}(U(h)_g - U(0)_g)}{m_{dust} v_r^{Maxwell}{}^2} \quad [8c]$$

525

526 The last term in Eq. (8a) on the right hand side, c_g , does not include effects of the Debye layer but only
 527 non-electromagnetic effects. Effects of the Debye layer are in the term c_ϕ which is the ratio between
 528 the electric potential of a dust particle within the Debye layer and the kinetic energy of a dust particle
 529 on the surface. If c_ϕ is larger than 1, the radial velocity is increased, and if c_ϕ is smaller than one the
 530 radial velocity is decreased by the Debye layer. Let us now consider the case when $c_\phi \gg c_g$ which can
 531 take place when the Debye layer is very narrow, the dust particle is light, the surface potential is strong
 532 or when the dust particle is strongly charged. In this case the initial radial velocity is changed by a factor
 533 of $\sqrt{1 + c_\phi}$ when it exits from the Debye sheath.

534

535 Table 1 gives the summary of the analysed 2D and 3D MC runs and the input parameters for the dust
 536 particles. It also shows the corresponding values for c_ϕ in the cases when the bulk velocity was non-
 537 zero.

538

539 The $(v_o, m/q)$ -phase space plot in Fig. 10 shows how c_ϕ depends on the (m/q) ratio of a positively
 540 charged dust particle with initial velocity v_o at the $SZA = 0^\circ$ case where the surface charge in the
 541 analysed PIC simulation was about +3 V on the surface (c.f. Fig. 4). Note that Figure 10 divides the $(v_o,$
 542 $m/q)$ -phase space into two regions. In the region $c_\phi < 0.1$ the contribution of the surface potential to
 543 the initial velocity is small because the acceleration is less than five percent ($\sqrt{1 + 0.1} = 1.0488$). In
 544 this parameter range the 3D density profile in the MC simulation depends on the initial velocity, and
 545 the PIC simulation results are not needed in the 3D MC simulation. In the region $c_\phi > 10$, instead, the
 546 role of the Debye layer is important because the radial velocity of a dust particle which has passed the
 547 layer is over three times the initial radial velocity ($\sqrt{1 + 10} = 3.3166$). In this range the PIC simulation
 548 forms a “link” in the DPEM model between the 3D hybrid model and the 3D MC models.

549

550 Figure 10 also illustrates how the six $(v_o, m/q)$ cases analysed in this paper differ from each other in
 551 terms of c_ϕ . Initial dust parameters on the Phobos and asteroid RQ36 cases are chosen in the region
 552 where the surface charging is important while the dust charging is not important in the analysed Moon
 553 case. The local 2D MC simulation was an “intermediate” case between the Phobos/asteroid RQ36 and
 554 the Moon cases. The dust cases analysed in this paper provide therefore examples of cases where the
 555 role of the surface charging varies. It should also be noted than in the MC model the surface charging
 556 was assumed to be zero on the nightside. According to Fig. 10 this can be interpreted as mimicking a
 557 situation where the phase space point $(v_o, m/q)$ was in the $c_\phi < 0.01$ region.

558

559 3.1 Charge and initial velocity of a dust particle

560 One highly critical yet unknown initial condition, which is needed to estimate properties of dust, in
 561 addition to the initial velocity of a dust particle, is the electric charge. It is illustrative to estimate what
 562 the charge of a dust particle on the object surface would be in the analysed surface electric field cases.

563 One way to estimate the charge of the surface and the dust on it is to assume that the charge is
 564 homogeneously distributed on a planar surface, that is, to assume there is a constant surface charge
 565 density σ [C/m²] on the surface of all material particles connected to the surface. If the electric field on
 566 the surface is E_{surf} then σ is equal to $2 \epsilon_0 E_{\text{surf}}$ according to Gauss' law. In the analysed SZA = 0° case
 567 $E_{\text{surf}} \sim +3$ V/m and, therefore, $\sigma \sim 5.31 \times 10^{-11}$ C/m² $\sim 3.3 \times 10^{-4}$ e/ μm^2 . This shows that only about less
 568 than one of every 10 thousand micron sized-dust particles has an electron while the other dust particles
 569 are non-charged.

570
 571 If we then assume that a spherical dust particle of the radius r_{dust} and the surface area of A_{dust} has the
 572 same surface charge density as the surface, the charge of the dust particle on the surface is
 573

$$574 q_{\text{dust}}[e] = A_{\text{dust}} \sigma = 4 \pi r_{\text{dust}}^2 \sigma \sim 0.0042 r_{\text{dust}}^2[\mu\text{m}] \quad [9]$$

576 Here the electric charge is given in the unit of the elementary charge e and the radius is given in μm . As
 577 Eq. 9 indicates, the charge of a dust particle is very small for a micron size particle in the analysed cases.
 578 For example, the radius of a dust particle has to be about 15 μm for the dust particle to carry the charge
 579 of an electron and about 150 μm to have a charge of 100 e , which is the order of the charge of a dust
 580 particle analysed in the paper. Such a particle would be very large and, consequently, very heavy. For
 581 example, if we assume a spherical dust particle with a mass density, $\rho_{\text{dust}}^{\text{mass}}$, of 3 g cm⁻³ the mass of a 1 e
 582 particle would be $\sim 3 \times 10^{16}$ amu and for a 100 e particle would be $\sim 3 \times 10^{19}$. This means that the
 583 $m_{\text{dust}}/q_{\text{dust}}$ ratio of a 1 e and a 100 e dust particle would be $\sim 3 \times 10^{16}$ amu/ e and $\sim 3 \times 10^{17}$ amu/ e ,
 584 respectively. Those high values are outside the range in Fig. 10 and belong to the region where the
 585 Debye layer is not important.

586
 587 The analysis suggests that if the surface is made of equal size spherical charged particles with size one
 588 micron or less, most of the dust particles would have zero charge. A more accurate estimation should
 589 take into account non-spherical shaped dust particles. A sphere is a geometrical shape where the
 590 surface area/volume ratio is in its minimum. Therefore, the mass of a non-spherical particle associated
 591 with the A_{dust} is smaller than for a spherical particle. It is, however, unlikely that a non-spherical “fluffy”
 592 shape of a particle could decrease the mass per charge ratio many orders of magnitude.

593
 594 Therefore, some other more effective dust charging mechanism than photoemission by EUV is needed
 595 to result in dust charges analysed in this paper if we assume a homogeneously distributed electric
 596 charge on a planar surface. Other surface charging sources could be X-rays [Manka, 1973] or
 597 micrometeoroid impact ionization (e.g. Collette et al., 2014). Secondary electrons also result in surface
 598 charging and their role has been studied widely, for example, when spacecraft charging has been
 599 analysed (e.g. Pavlík et al. 2014). Laboratory measurements have shown that dust particles are
 600 mobilized and transported on the surface near regions of differing secondary electron yields due to
 601 either their characteristic compositions or surface roughness, and that a few kV/m electric field can be
 602 formed near the surface [Wang et al., 2010]. However, it is not clear how well the laboratory
 603 measurements can mimic real situations on the lunar surface. Moreover, the question of how large the
 604 charge of a dust particle can be and what mechanism could lift dust particles from the surface is
 605 unknown.

606

607 The phase space shown in Figure 10 illustrates the parameter range where the surface charging can
608 have global effects on dust densities, i.e., when surface charging has substantial effects on the velocity
609 of a dust particle after it has escaped from the Debye layer. However, it is also informative to analyse
610 local effects, that is, a situation when the initial velocity of a dust particle is large enough to affect its
611 motion within the Debye layer. It is interesting to look how small a dust particle on a surface can be so
612 that after emission of the minimum amount of electric charge, i.e., one photoelectron, it would have
613 such a small m/q ratio that the surface potential would be important. If we assume again that the mass
614 density of a spherical dust particle is 3 g cm^{-3} , the radius of a particle which has emitted one
615 photoelectron and which m/q ratio is $1 \times 10^{11} \text{ amu/e}$, $1 \times 10^{10} \text{ amu/e}$, $1 \times 10^9 \text{ amu/e}$ and $1 \times 10^8 \text{ amu/e}$ is
616 $\sim 0.2 \text{ }\mu\text{m}$, $\sim 0.1 \text{ }\mu\text{m}$, $\sim 0.05 \text{ }\mu\text{m}$, and $\sim 0.02 \text{ }\mu\text{m}$, respectively. According to Fig. 10 those particles are
617 close to the $c_\phi = 1$ line if their initial radial velocity is of the order of $\sim 0.06 \text{ km/s}$, $\sim 0.3 \text{ km/s}$, ~ 0.8
618 km/s , $\sim 3 \text{ km/s}$, respectively. This implies that for a dust particle of radius, say, $\sim 0.02 \text{ }\mu\text{m}$ the initial
619 velocity becomes locally important if it is of the order of 1 km/s , as demonstrated in 1D PIC
620 simulations which showed that the maximum velocity of a levitating $0.02 \text{ }\mu\text{m}$ dust particle is only few
621 m/s (see Poppe and Horányi, 2010, Fig. 11). However, it is not known how a dust particle could have
622 an initial velocity of the order of km/s .
623

624 4. Discussion

625
626 This paper describes the new unified DPEM modelling suite to analyse dust and plasma near an airless
627 object locally and globally by three kinetic models. The 3D hybrid model uses a hybrid model package
628 built on the publicly available FLASH code (<http://flash.uchicago.edu/site/flashcode/>), which has
629 already been used to study the Moon-solar wind interaction [Holmström et al., 2012]. The 3D MC
630 model was also built around the FLASH code, and it uses a new dust software package developed for
631 the DPEM model. The PIC model is a new code utilising the HYB software platform, which included
632 initially a hybrid model (e.g. Kallio, 2005, and references therein), a 3D electromagnetic model, and
633 then a 1D electrostatic model. Recently, the developed 2D PIC model has been extended to model also
634 a non-planar surface [Dyadechkin et al., 2015].
635

636 The DPEM model provides a tool to analyse many aspects associated with the plasma and dust near
637 the surface of an airless body, such as [1] the properties of plasma near the surface based on a 3D
638 kinetic model (hybrid model), [2] to study electric potential and the dust density profiles within and
639 near the surface (PIC model) and, finally, [3] to obtain 3D dust density profiles. The analyses imply that
640 properties of the lifted dust strongly affect the dust densities locally and globally depending on the
641 mass, charge and initial velocity of the dust.
642

643 Although the DPEM model links three individual models, which are dedicated to analysing different
644 plasma processes and plasma phenomena, the modelling suite can be regarded as the first step towards
645 a real unified model for studying the dust environment of airless bodies. The one direction connection
646 between the models Hybrid→PIC→MC (c.f. Fig. 1) manifests the challenge of the physical processes
647 in a wide range of space and time scales. The fastest processes in the modelling suite are the electron
648 plasma frequency ($\sim 9 \sqrt{n_e[\text{cm}^{-3}]} \text{ kHz}$) and the smallest space scale is the Debye length ($\sim 69 \sqrt{T_e[\text{K}]/n_e[\text{m}^{-3}]} \text{ m}$)
649 that are considered in the PIC model. Therefore, for example, in the PIC model the
650 time step in the simulation, the running time, and the grid size were $5 \times 10^{-8} \text{ s}$, 2 ms and 0.25 min ,
651 respectively. These values were much smaller than those used in the MC model, which considered the
652 slowly moving dust particles in a 3D space. For example, in Figs. 6-9 the running time of the simulation
653 was thousands of seconds.
654

655 Because of the highly different time and space scales in the three DPEM models, dust particles did not
656 affect the properties of plasma in the PIC or hybrid model. In a completely unified model, instead, the
657 link in a dusty-plasma model should be two way (Hybrid \square PIC \square MC). For example, dust particles can
658 be a source of electrons, the so called dust electrons (e.g. Stubbs et al., 2011), which in turn affect the
659 electron density and electron distribution function. A self-consistent model should include this effect
660 into the PIC model. Moreover, the charge of a dust particle above the surface varies in time and it
661 depends on the nearby plasma (see e.g. Nitter et al., 1998) while the charge of a dust particle was kept
662 constant in the 2D PIC simulation (c.f. Fig. 5) and in the 3D MC simulations (c.f. Figs. 6-9) for
663 simplicity. It is however a very challenging task to model the whole system fully self-consistently with
664 present computational resources.

665
666 The night-side region was also modelled in a simpler manner by using a zero surface potential. This
667 approach was chosen because the hybrid model does not give accurate plasma parameters near the
668 surface by or at midnight. It can be envisioned that a more realistic 3D dust distribution could be
669 obtained when the PIC model uses, for example, observations or some other models. In addition, 2D
670 landscapes can affect the electric potential and they should be included into the PIC model (see e.g.
671 Zimmerman et al., 2011). Lunar magnetic anomalies also affect the properties of the precipitating solar
672 wind protons and the electric potential near the surface (see, e.g. hybrid modelling by Jarvinen et al.,
673 2014). In the future, such magnetic field regions could be simulated with the DPEM model by
674 combining the 3D hybrid model which simulates magnetic anomaly globally and a local PIC simulation
675 which gives electric potential within the Debye layer.

676
677 It should also be mentioned, that although the DPEM model enables to derive detailed knowledge of
678 the properties of the solar wind protons near the terminator region, which can in turn be used in the
679 PIC simulation, in the analysed cases that detailed information was not used in the PIC model. This
680 choice was done because the level of disturbance was relatively small (c.f. Fig 3). However, if the goal
681 of the study would have been to analyse local property of the dust near the terminator region, for
682 example, near the lunar polar regions, the detailed velocity distribution function obtained from the
683 hybrid model would have been highly valuable. It would also be interesting to test how the properties
684 of the plasma differ near the terminator region at different solar wind conditions and, for example,
685 when the Moon is the Earth's magnetosphere or when Phobos is in the induced Martian
686 magnetosphere. Moreover, the hybrid model can also simulate cases when the solar wind plasma is
687 non-Maxwellian. Such studies are, however, beyond the scope of the present work.

688
689 When the presented results are interpreted one should also recall that the DPEM suite does not contain
690 a model of how dust particles are initially injected from the surface. In other words, the DPEM model
691 does not include information of how many dust particles are emitted at various places in the (v_{∞} , m/q)-
692 phase space shown in Fig. 10. Therefore, the DPEM modelling suite cannot provide absolute dust
693 density profiles without inclusion of an additional dust lifting model, based on the laboratory
694 measurements on hypervelocity impacts, for example (see e.g. Frisch, 1992; Eichhorn and Grün, 1993;
695 Lange and Ahrens, 1987), or dust lifting models based on the first physical principles of the forces
696 affecting dust particles on the surface of an airless body (see e.g. Hartzell and Scheeres, 201; Hartzell,
697 2012). For example, as can be seen in Fig. 10, the initial parameters of the dust particles injected from
698 the surface of RQ36 (Fig. 6-7) and Phobos (Fig. 8) were chosen in the phase space so that the surface
699 electric potential has a significant contribution to the density of dust.

700
701 Modelling is also complicated due to the fact that the shape and surface area of the dust particles are
702 highly irregular and relatively large, respectively (e.g. Liu et al., 2008 and Liu and Taylor, 2011). These
703 would be crucial input parameters to obtain a realistic 3D dust density profile. Therefore, more
704 theoretical studies and laboratory measurements are called for to characterise more precisely the
705 properties of lifted dust particles. Moreover, different lunar missions and different observations have

706 provided contradictory results about the properties of dust around the Moon (see e.g. Feldman et al.,
707 2014) and, therefore, more dedicated remote sensing and *in situ* dust observations are needed. This will
708 help in further understanding the interaction of the charged particles and the potential “dangling”
709 surface bonds (free radicals) with the exterior and interior of the human body (e.g. Fubini and
710 Hubbard, 2003; and Hurowitz et al., 2007) and technical instrumentation used on the lunar surface.
711 This will enable a better understanding of the potential toxicity of the lifted dust particles and
712 respective hazards to human health. Moreover, the improvements in models can also help better
713 protect scientific and technical instrumentation used on the lunar surface.
714
715

716 5. Summary

717
718 A new tool called the DPEM modelling suite has been developed to study dust environments of airless
719 objects. The unified kinetic model was used to study three different object sizes (the Moon, the Martian
720 moon Phobos and the asteroid RQ36). The phase space analysis revealed the region in the initial
721 velocity - the mass-to-charge ratio phase space where the density of the dust particles was affected
722 strongly by the electric field within the Debye layer. The study also showed how the 3D density
723 distribution of such dust particles is affected by the Debye layer. Overall, the initial results presented in
724 this paper suggested that when a realistic dust emission model is available, the unified DPEM modelling
725 suite provides a powerful tool to study the dust environments of airless bodies such as moons,
726 Mercury, asteroids and non-active comets far from the Sun.
727
728
729

730 Acknowledgements

731 The authors acknowledge the ESA GSP program project DPEM, Dusty plasma environments: near-
732 surface characterization and modelling (ESA IIT, AO-1-6696/11/NL/CO) for the financial support
733 for the work. The authors thank Fabrice Cipriani/ESTEC/ESA for the discussions about dusty
734 plasma. Authors would like to acknowledge Dr. D. Kent Ross (NASA-JSC) for proofreading the
735 manuscript and for useful comments and remarks. EK thanks Dr. Cyril Simon Wedlund, Aalto
736 University, for useful suggestions about the manuscript. Figs. 2, 6, 7, 8 and 9 are made by the VisIt
737 visualization tool.
738
739

740 References

- 741
742 Cain J. R., Lunar dust: the hazard and astronaut exposure risks, 2010, Earth, Moon, Planets 107, 107-
743 125.
744
745 Collette, A., E. Grün, D. Malaspina, Z. Sternovsky, 2014, Micrometeoroid Impact-Charge Yield for
746 Common Spacecraft Materials, J. Geophys. Res., doi: 10.1002/2014JA020042.
747
748 Dyadechkin, S., E. Kallio, and P. Wurz, 2015, New fully kinetic model for the study of electric
749 potential, plasma, and dust above lunar landscapes, J. Geophys. Res. Space Physics, 120,
750 doi:10.1002/2014JA020511.
751

752 Eichhorn, K. and G. Eberhar, 1993, High-velocity impacts of dust particles in low-temperature water
753 ice, *Planetary and Space Science*, Volume 41, Issue 6, pp. 429-433, doi:10.1016/0032-0633(93)90002-J.
754

755 Farrell, W.M., Stubbs, T.J., Vondrak, R.R., Delory, G.T., Halekas, J.S., 2007, Complex electric fields near
756 the lunar terminator: the near-surface wake and accelerated dust, *Geophysical Research Letters*
757 34, L14201, <http://dx.doi.org/10.1029/2007GL029312>.
758

759 Feldman P. D., D. A. Glenar, T. J. Stubbs, K. D. Retherford, R. Gladstone, P. F. Miles, T. K.
760 Greathouse, D. E. Kaufmann, J. Wm. Parker, S. A. Stern, 2014, Upper limits for a lunar dust
761 exosphere from far-ultraviolet spectroscopy by LRO/LAMP, *Icarus* 233, pp. 106–113.
762

763 Frisch, W., 1992, Hypervelocity impact experiments with water ice targets in *Hypervelocity Impacts in*
764 *Space*, Edited by McDonnell. J. A. M., pp. 7-14. Unit for Space Sciences, University of Kent.
765

766 Fubini B. and Hubbard A., 2003, Serial Review: Role of Reactive Oxygen and Nitrogen Species
767 (ROS/RNS) in Lung Injury and Diseases. *Free Radical Biology & Medicine* 34, 1507–1516. Holmström,
768 M., Fatemi, S., Futaana, Y., Nilsson, H., 2012, The interaction between the Moon and the solar wind,
769 *Earth, Planets and Space* 64, 237–245, <http://dx.doi.org/10.5047/eps.2011.06.040>.
770

771 Hartzell, C. M. and D. J. Scheeres, 2011, The role of cohesive forces in particle launching on the Moon
772 and asteroids, *Planetary and Space Science* 59, pp. 1758–1768.
773

774 Hartzell, C., 2012, The dynamics of near-surface dust on airless bodies, Ph.D. Thesis, University of
775 Colorado.
776

777 Hurowitz J.A., Tosca N.J., McLennan S.M. and Schoonen M.A.A., 2007, Production of hydrogen
778 peroxide in Martian and lunar soils. *Earth and Planetary Science Letters* 255, pp. 41–52.
779

780 Jarvinen, R., M. Alho, E. Kallio, P. Wurz, S. Barabash, and Y. Futaana, 2014, On vertical electric fields
781 at lunar magnetic anomalies, *Geophys. Res. Lett.*, 41, 2243–2249, doi:10.1002/2014GL059788,
782

783 Kallio, E., J. G. Luhmann, and S. Barabash, 1997, Charge exchange near Mars: The solar wind
784 absorption and neutral atom production, *J. Geophys. Res.*, 102, 22, 183-22, 197.
785

786 Kallio, E., Formation of the lunar wake in quasi-neutral hybrid model, 2005, *Geophysical Research*
787 *Letters*, 32, L06107, <http://dx.doi.org/10.1029/2004GL021989>.
788

789 Kallio, E., R. Jarvinen, S. Dyadechkin, P. Wurz, S. Barabash, F. Alvarez, V. Fernandes, Y. Futaana, J.
790 Heilimo, C. Lue, J. Makela, N. Porjo, W. Schmidt and T. Siili, 2012, Kinetic simulations of finite
791 gyroradius effects in the lunar plasma environment on global, meso, and microscales, *Planetary and*
792 *Space Science*, <http://dx.doi.org/10.1016/j.pss.2012.09.012>.
793

794 Kallio, E. and G. Facskó, Properties of plasma near the Moon in the magnetotail, *Planetary and Space*
795 *Science*, doi:10.1016/j.pss.2014.11.007, 2015.
796

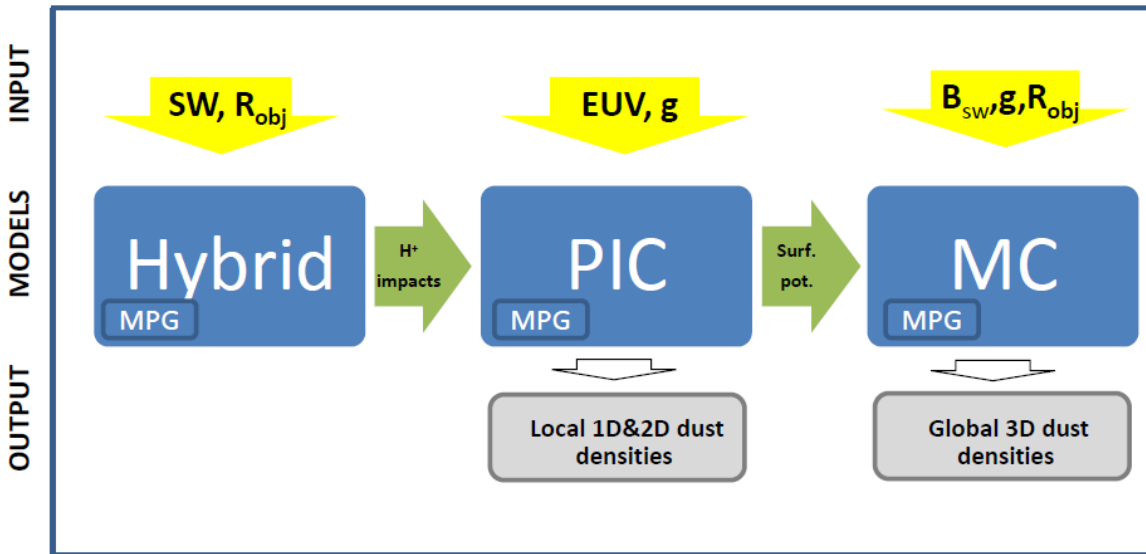
797 Dyadechkin, S., E. Kallio, P. Wurz, 2015, New fully kinetic model for the study of electric potential,
798 plasma and dust above lunar landscapes, *J. Geophys. Res.*, DOI: 10.1002/2014JA020511,
799

800 Jordan, A. P., T. J. Stubbs, J. K. Wilson, N. A. Schwadron, and H. E. Spence, 2015, Dielectric
801 breakdown weathering of the Moon's polar regolith, *J. Geophys. Res. Planets*, 120, 210–225,

802 doi:10.1002/2014JE004710.
803
804 Lange, M. A. and T. J. Ahrens, 1987, Impact experiments in low-temperature ice, *Icarus*, Volume 69,
805 Issue 3, pp. 506–518, doi:10.1016/0019-1035(87)90020-0
806
807 Linnarsson, D., J. Carpenter, B. Fubini, P. Gerde, L. L. Karlsson, D. J. Loftus, G. K. Prisk, U. Staufer,
808 E. M. Tranfield and W. van Westrenen, 2012, Toxicity of lunar dust, *Planetary and Space Science* 74,
809 57–71.
810
811 Liu Y. and Taylor T. A., 2011, Characterization of lunar dust and a synopsis of available lunar
812 simulants. *Plan. Space Sci.* 59, 1769–1783.
813
814 Liu Y., Park J. S., Schnare D., Hill E. and Taylor L. A., 2008, Characterization of lunar dust for
815 toxicological studies: Part 2-morphology and physical characteristics. *J. Aerosp. Eng.* 21, 272–279.
816
817 Manka, R.H. Plasma and potential at the lunar surface, 1973, in: Grard, R.J.L. (Ed.), *Photon and*
818 *Particle Interactions with Surfaces in Space*. D. Reidel Publishing Co., Dordrecht, Holland, pp. 347–
819 361.
820
821 Murphy, D.L., Vondrak, R.R., 1993, Effects of levitated dust on astronomical observations from the
822 lunar surface. *Proc. Lunar Planet. Sci. Conf.* 24th, 1033–1034.
823
824 Nitter, T., Havnes, O., Melandso, F., 1998, Levitation and dynamics of charged dust in the
825 photoelectron sheath above surface in space, *J. Geophys. Res.*, 103(A4), 6605–6620,
826 <http://dx.doi.org/10.1029/97JA03523>.
827
828 Pavlík, J., M. Beránek, J. Vaverka, J. Šafránková, Z. Nemeček, and I. Richterová, 2014, Secondary
829 electron emission from Martian soil simulant, *J. Geophys. Res. Planets*, 119, 199–209,
830 doi:10.1002/2013JE004522.
831
832 Poppe, A., and M. Horányi, 2010, Simulations of the photoelectron sheath and dust levitation on the
833 lunar surface, *J. Geophys. Res.*, 115, A08106, doi:10.1029/2010JA015286.
834
835 Stubbs T. J., Vondrak R. R. and Farrell W. M., 2006, A dynamic fountain model for lunar dust. *Adv.*
836 *Space Res.* 37, pp. 59–66, 65.
837
838 Stubbs, T.J., Glenar, D.A., Farrell, W.M., Vondrak, R.R., Collier, M.R., Halekas, J.S., Delory, G.T.,
839 2011, On the role of dust in the lunar ionosphere, *Planetary and Space Science*,
840 <http://dx.doi.org/10.1016/j.pss.2011.05.011>.
841
842 Wang, X., Horányi, M., Robertson, S., 2010, Investigation of dust transport on the lunar surface in a
843 laboratory plasma with an electron beam. *J. Geophys. Res.* 115, A11102, pp. 1–6.
844
845 Willis, R. F., M. Anderegg, B. Feuerbacher, and B. Fitton, 1973, Photoemission and secondary electron
846 emission from lunar surface material, in *Photon and Particle Interactions With Surfaces in Space*, edited
847 by R. J. L. Grard, pp. 369–387, Springer, New York.
848
849 Zimmerman, M. I., W. M. Farrell, T. J. Stubbs, J. S. Halekas, and T. L. Jackson, 2011, Solar wind access
850 to lunar polar craters: Feedback between surface charging and plasma expansion, *Geophys. Res. Lett.*,
851 38, L19202, doi:10.1029/2011GL048880.
852

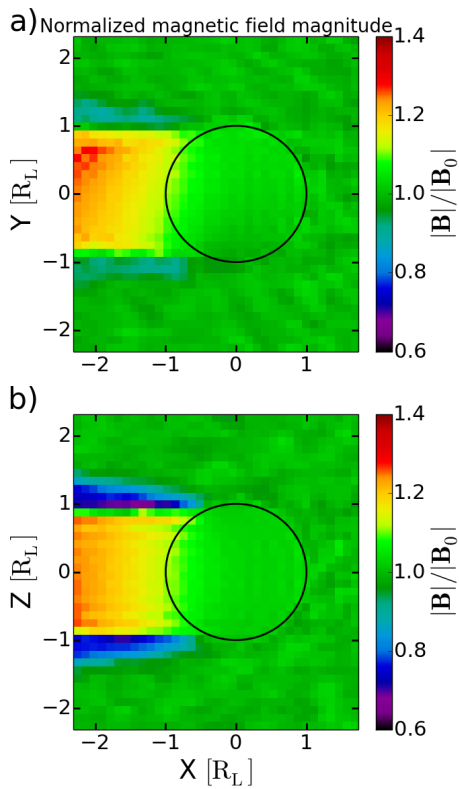
854 **Figure Captions**

855
856
857

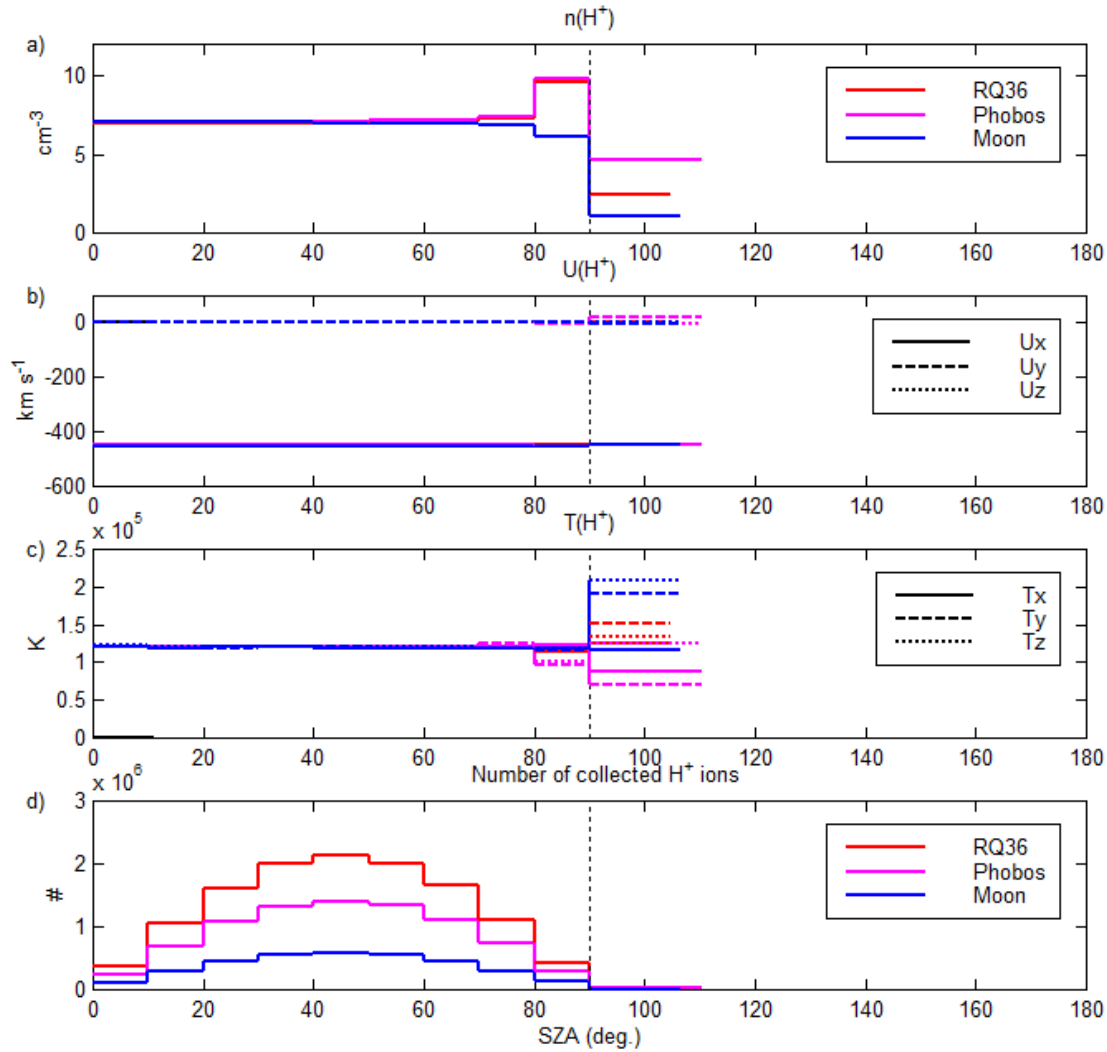


858
859
860
861
862
863
864
865
866
867
868
869
870
871
872

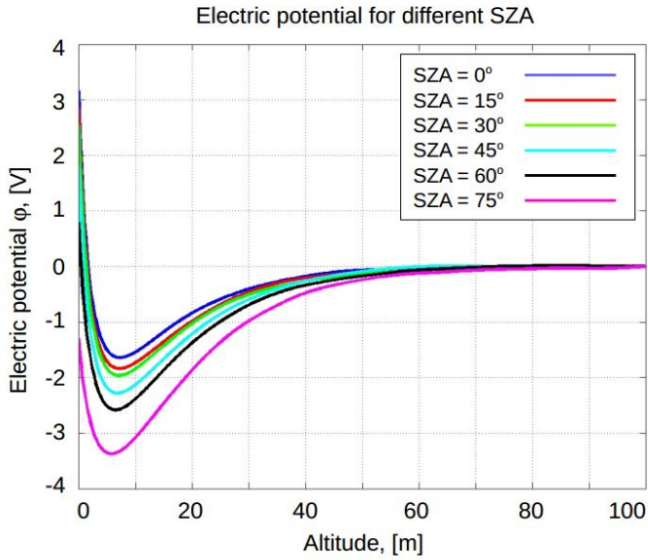
Figure 1. Overview of the three models in the DPEM modelling suite: [1] a 3D Hybrid model, [2] a 2D electrostatic full kinetic Particle-In-Cell (PIC) model, and [3] a 3D Monte Carlo (MC) model. All three models have also their own 3D Maxwellian Particle Generator, MPG, to inject particles into models. Models are connected to each other by a one-way connection: The PIC model uses the impacting H⁺ ions derived by the hybrid model while the MC model uses the surface potential calculated by the PIC model. Input parameters for the models are the solar wind (SW), the radius of the object (R_{obj}), the gravitational force (g) and the interplanetary magnetic field (B_{sw}). The physical output dust parameters are 1D, 2D and 3D density profiles.



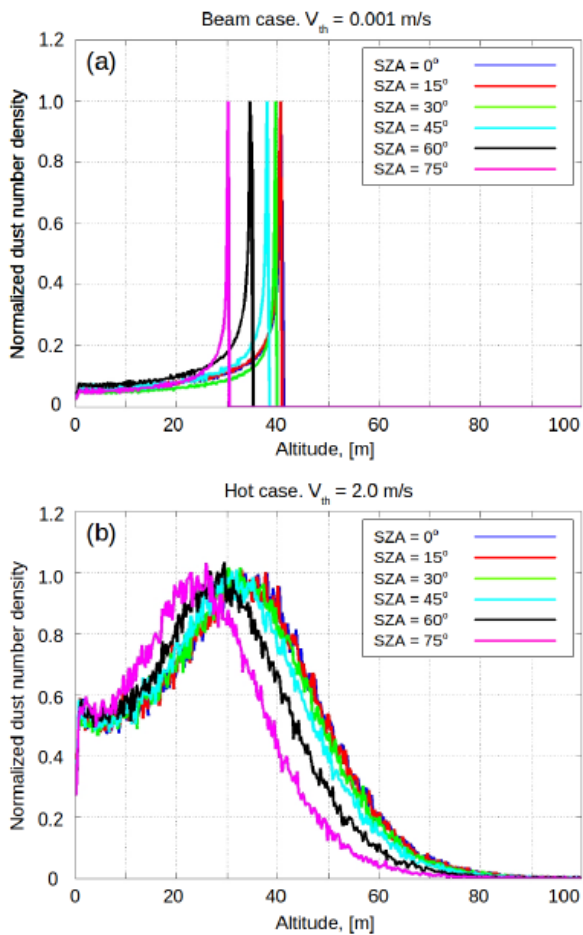
873
 874 Figure 2. An example of a run made by the DPEM hybrid model. The colour gives the magnitude of
 875 the magnetic field normalized by the undisturbed magnetic field on two planes: (a) on the $z=0$ plane
 876 and (b) on the $y=0$ plane. The solar wind flows in the figure from right to left and the Moon is assumed
 877 to be in the undisturbed solar wind.
 878
 879
 880
 881



882
 883 Figure 3. Macroscopic properties of the H^+ protons precipitating on the surface of the Moon (blue
 884 lines), Phobos (magenta lines), and asteroid RQ36 (red lines). In panels b) and c) the solid, dash-dot
 885 and the dotted lines show the x, y and z components, respectively. The bottom panel shows the
 886 number of precipitated H^+ ions on the surface into 10° intervals of the SZA. The vertical dotted line at
 887 $SZA=90^\circ$ shows the position of the terminator plane which separated the dayside and nightside
 888 hemispheres. Note that in panel d) the maximum number of collected particles is obtained in the region
 889 $40^\circ < SZA < 50^\circ$ because the area of that ring on the lunar surface perpendicular to the flow of the
 890 solar wind is larger than the perpendicular area in other 10° intervals.
 891
 892



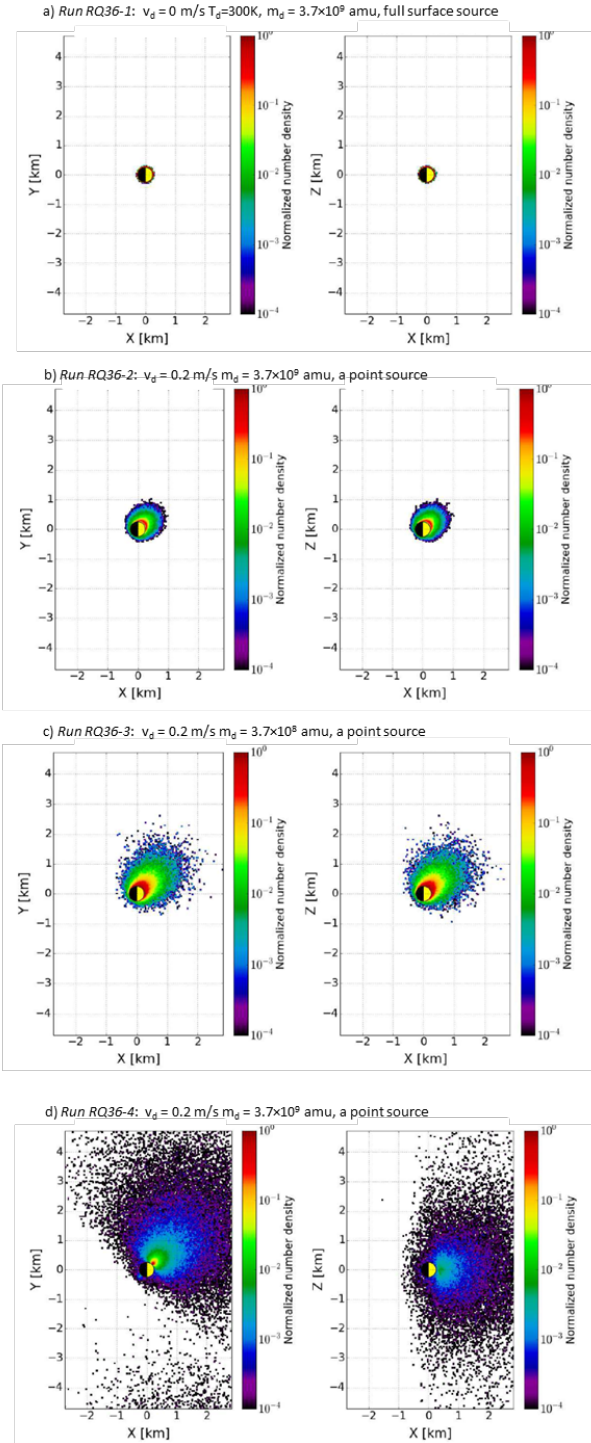
893
 894 Figure 4. 1D profiles of the electric potential derived from a 1D electrostatic PIC simulation for six
 895 SZA values.
 896



897
 898
 899
 900
 901
 902 Figure 5. Analysis of the role of the surface charging to the density of dust within the Debye layer. The
 903 curves show the normalized density of dust particles at six SZA cases for the (a) “cold” dust run (*the*

904 *Run PIC-1*) and (b) the “hot” dust run (*the Run PIC-2*) when the thermal velocity (V_{th}) was small, large
 905 compared with the bulk velocity, respectively. The densities are calculated with the 2D MC model by
 906 using the electric potential given in Fig. 4. In (a) every six cases are normalized so that the maximum
 907 density is one. In (b) densities are normalized with the maximum density of dust in the $SZA = 0^\circ$ case.
 908
 909

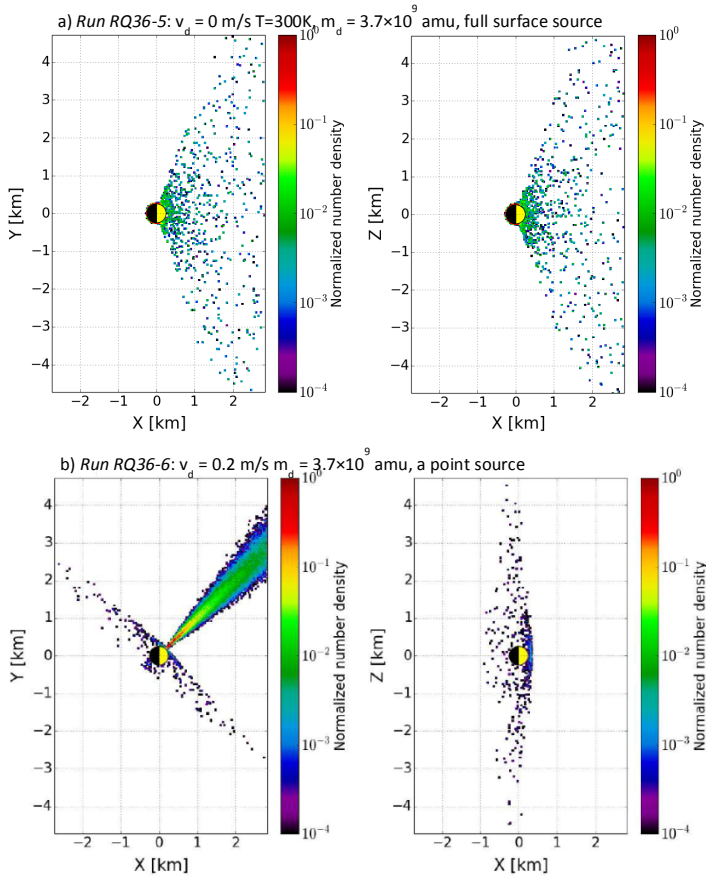
Asteroid RQ36 (no surface charge)



910
 911
 912 Figure 6. Normalized dust densities around asteroid RQ36 on the (left columns) XY-plane and (right
 913 columns) on the XZ-plane when the surface potential is not included. In the first run (*RQ36-1*) dust

914 was emitted from the full surface while in the rest three runs (*RQ36-2*, *RQ36-3*, *RQ36-4*) dust was
 915 emitted from a single point. Legends of the panels show the input parameters: The initial velocity (v_d)
 916 or temperature (T_d) of a dust particle and its mass (m_d). In all cases the charge of the dust particle was
 917 $+350 e$. The densities in panels a), b), c) and d) are snapshots at 6000 s, 7500 s, 7500s and 7500 s after
 918 the continuous emission was started, respectively. In the plots the Sun is on the right.
 919
 920

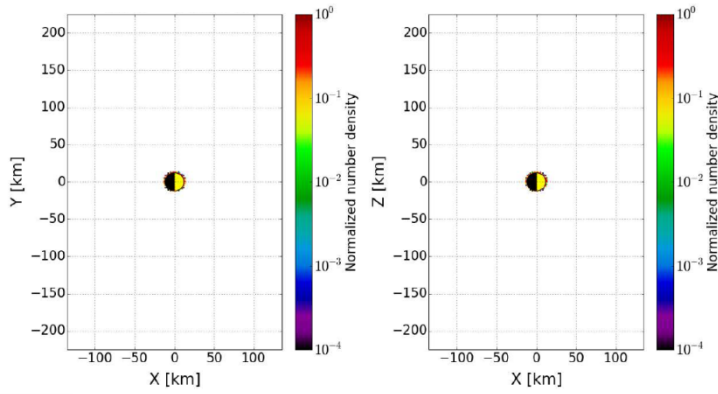
Asteroid RQ36 (surface charge included)



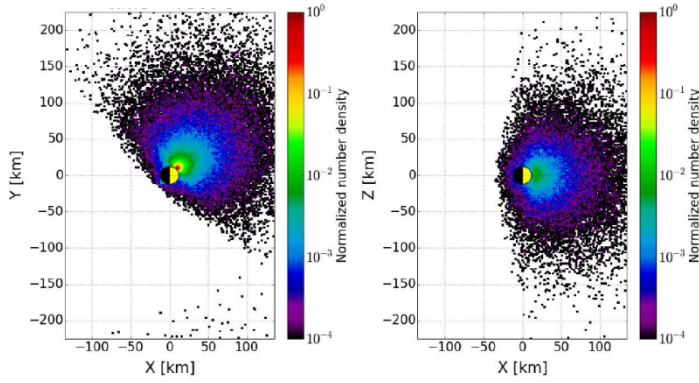
921
 922 Figure 7. Normalized dust densities around asteroid RQ36 on the (left columns) XY-plane and (right
 923 columns) on the XZ-plane when the surface potential is included. The run on the top (*RQ36-5*)/bottom (*RQ36-6*) is otherwise similar than the Run *RQ36-1*/
 924 *RQ36-4* shown in Fig. 6. The densities in panels a) and b), are snapshots at 6000 s and 7500 s after the continuous emission was started,
 925 respectively. In the plots the Sun is on the right.
 926
 927
 928

Phobos

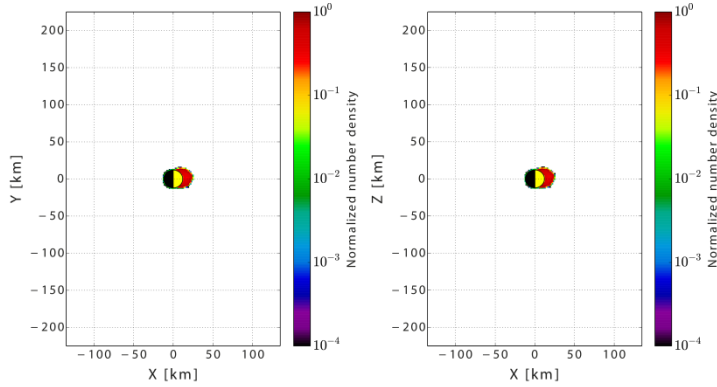
a) *Run Phobos-1*: $v_d = 0$ m/s $T_d = 300$ K, $m_d = 3.7 \times 10^9$ amu, full surface source, no surf. charging



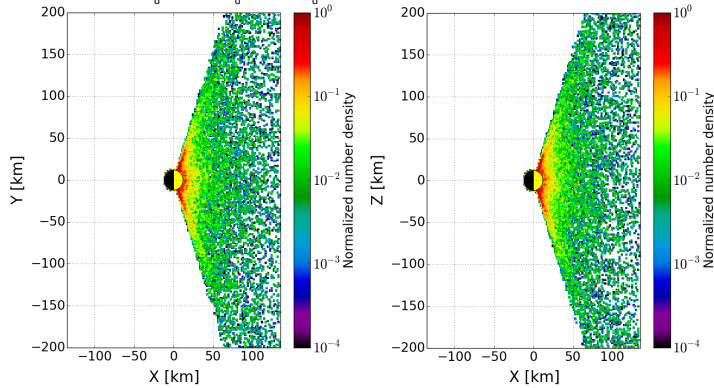
b) *Run Phobos-2*: $v \sim 11$ m/s $m = 3.7 \times 10^9$ amu, a point source, no surf. charging



c) *Run Phobos-3*: $v_d = 0$ m/s $T_d = 300$ K, $m_d = 3.7 \times 10^9$ amu, full surface source, with surf. charging

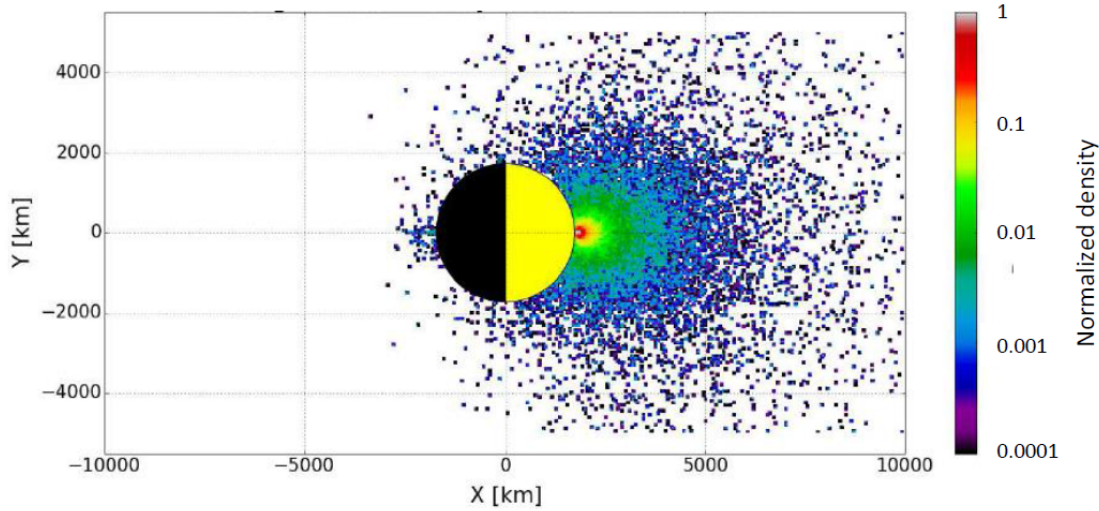


d) *Run Phobos-4*: $v_d = 0$ m/s $T_d = 300$ K, $m_d = 3.7 \times 10^8$ amu, full surface source, with surf. charging

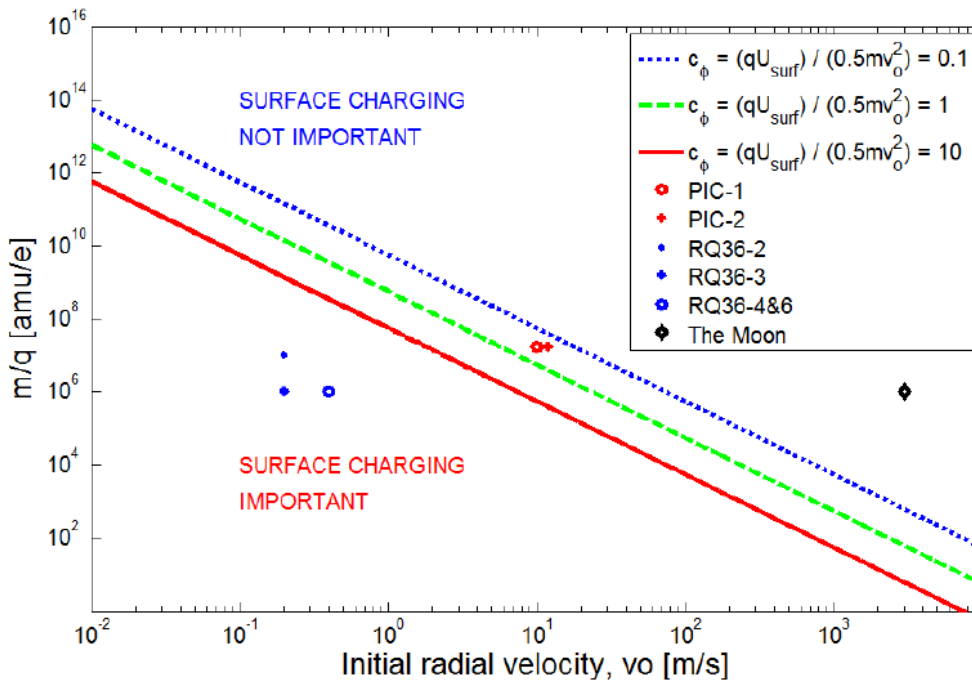


930 Figure 8. Normalized dust densities around Martian moon Phobos on the (left columns) XY-plane and
 931 on the (right columns) XZ-plane at four MC model runs. In panels a) and b) there is no surface
 932 charging but in panels c) and d) the surface charging is added. Dust was emitted from the full surface in
 933 panels a) and c) and d) while the panel b) shows the point source situation. The densities in panels a),
 934 b), c) and d) are snapshots at 10000 s, 7500 s, 10000 s and 40000 s after the continuous emission was
 935 started, respectively. In the plots the Sun is on the right.
 936

The Moon



937
 938
 939 Figure 9. Normalized dust densities around the Moon on the XY-plane derived from the 3D MC
 940 simulation. Dust particles were emitted at the subsolar point ($SZA = 0^\circ$). The densities are derived after
 941 5000 s (~ 1.4 h) continuous dust emission.
 942



943
 944
 945 Figure 10.

946 The $(v_o, m/q)$ -phase space where the analysed dust simulations are marked in the 2D phase space
 947 according to the initial velocity (v_o) and the initial mass per charge (m/q) ratio of the dust particles. The
 948 ratio (c_ϕ) of the electric potential energy of a positive dust particle to the vertical kinetic energy at
 949 different (m/q) and initial radial velocity (v_o). The three lines present $c_\phi = 0.1, 1, \text{ and } 10$ cases. The
 950 marks represent six initial ($v_o, m/q$) parameter pairs used in the local 2D simulation with the Debye
 951 layer (Runs PIC-1 and PIC-2) and in the 3D MC simulations for the Phobos moon, the asteroid RQ36,
 952 for the Moon simulation.

953
 954
 955
 956
 957
 958

Tables

Name of the run	Object	m_{dust} (amu)	Surf. charg. included	q_{dust}	U_{dust}	T_{dust} or $U_{\text{dust}}^{\text{therm}}$	$c_\phi \equiv \frac{E_\phi^{\text{pot}}}{E_r^{\text{kin}}}$	Dust source
PIC-1	The Moon	3.76×10^9	Yes	+221e	10 m/s	1 mm/s	0.3	entire surface
PIC-2	The Moon	3.76×10^9	Yes	+221e	10 m/s	2 m/s	0.2	entire surface
RQ36-1	RQ36	3.7×10^9	No	+350 e	0 m/s	300 K		entire surface
RQ36-2	RQ36	3.7×10^9	No	+350 e	0.2 m/s	300 K	1.4×10^3	point
RQ36-3	RQ36	3.7×10^8	No	+350 e	0.2 m/s	300 K	1.4×10^4	point
RQ36-4	RQ36	3.7×10^8	No	+350 e	0.4 m/s	300 K	3.4×10^3	point
RQ36-5	RQ36	3.7×10^9	Yes	+350 e	0 m/s	300 K		entire surface
RQ36-6	RQ36	3.7×10^8	Yes	+350 e	0.4 m/s	300 K	3.4×10^3	point
Phobos-1	Phobos	3.7×10^9	No	+350 e	0 m/s	300 K		entire surface
Phobos-2	Phobos	3.7×10^9	No	+350 e	0 m/s	300 K		point
Phobos-3	Phobos	3.7×10^9	Yes	+350 e	0 m/s	300 K		entire surface
Phobos-4	Phobos	3.7×10^8	Yes	+350 e	0 m/s	300 K		entire surface
The Moon	The Moon	3.7×10^9	No	+350 e	3 km/s	300 K	6.0×10^{-5}	entire surface

959
 960
 961
 962
 963
 964
 965
 966
 967
 968
 969

Table 1. Summary of the analysed MC runs and the input parameters used for the dust particles. The dust is emitted from the surface with a 3D Maxwellian velocity distribution function with the radial bulk velocity (U_{dust}) and temperature (T_{dust}) or the thermal speed ($U_{\text{dust}}^{\text{therm}}$). The second last column on the left is a parameter c_ϕ which represents the role of the surface charge in Eq. 8b. The charge and the mass of the dust particle is given in elementary charge (= the charge of an electron) and atomic mass unit, amu, (\sim the mass of a proton), respectively. The velocity used to calculate c_ϕ in the PIC-2 run was taken to be 12 m/s ($=U_{\text{dust}} + U_{\text{dust}}^{\text{therm}}$) for simplicity. Values c_ϕ are derived for the surface potential +3 V which is the case near the subsolar point in the analysed input parameter cases.